TÉCNICO LISBOA

On the Uncertainty Quantification of the Unsteady Aerodynamics of 2D Free Falling Plates

Nicola Zorzi

November 2013

Abstract

The free fall of two-dimensional cards immersed in a fluid was studied using a deterministic and stochastic numerical approach. The motion is characterized by the fluid-body interaction described by coupling the Navier-Stokes and rigid body dynamic equations. The model's predictions have been validated using both the experimental and numerical data available in literature.
In the stochastic simulations, the fillet radius of the plate was considered a random variable characterized by a uniform Probability Density Function (PDF) introducing, in this way, some uncertainties in the plate's trajectory. To take into account the uncertainties we employed the Non-Intrusive Spectral Projection (NISP) method based on polynomial chaos expansion. The analysis was focused on finding the ensemble mean trajectory and error bar for a confidence interval of 95% for both tumbling and fluttering regimes.

Keywords: Falling plate, Fluttering, Tumbling, Uncertainty Quantification, Stochastic analysis

1 Introduction

We all know that a falling leaf does not reach the ground with a straight vertical trajectory but a graceful and elegant path is drawn in the air. Similarly, tree seeds, business cards, or common sheets of paper, fall down swinging from side to side regularly (fluttering), moving sidewise and spinning on an axis (tumbling), or they can also have more complicated three dimensional motions [1].
The study of falling strips of paper started with Maxwell in 1854 [2], even before the development of the aerodynamic theory, with a qualitative description of the tumbling phenomena. Dupleich [3] analysed the characteristics of motion of several body shapes dropped in different conditions. He noticed that in some specific geometrical conditions, periodic-oscillating motion (fluttering) appears. Lugt [4, 5] conducted both experimental and numerical research recognizing the big role played by the plate vortex shedding.
In 1998, Belmonte *et al.* [6] studied the transition from fluttering to tumbling in a quasi-two-dimensional experiment in which flat strips were dropped in a narrow container filled with fluid whereby the mechanical constraints ensured the two-dimensional plate motion. Further improvements were done by Andersen *et al.* [7] who eliminated the mechanical constrains and used a release mechanism for dropping the aluminium plates. By using a high-speed digital video they determined the instantaneous acceleration and thus the instantaneous forces acting on the plate.
In the last decade, free falling phenomena has been investigated using CFD. In general, numerical simulation of freely falling body is not a simple problem: it requires models with unsteady aerodynamics and moving solid boundaries that need large computational capacities. In addition, a fluid-body interaction study is required: the plate is considered perfectly rigid but the trajectory is the results of the combined action of both the fluid forces and the gravitational ones. In this direction Mittal *et al* [8] solved directly the 2D Navier-Stokes equations for both fixed and free axes plate. In his analysis he found that the plate has an increase tendency to tumble when the Reynolds number increases and the thickness ratio decreases. Pesavento & Wang [9] solved the 2D Navier-Stokes equations for the flow around tumbling plate in the vorticity stream function formulation using an elliptical body in order to avoid the singularities caused by the conformal mapping technique. Andersen *et al.* [7], using the same mathematical formulation, qualitatively compared the numerical solution, for both tumbling and fluttering cases, with the experimental one measured in the same paper and ascribed the discrepancies to the the geometrical body differences (in the experiments, rectangular cross section was used). Later, in 2008, Jin & Xu [10] tried to overcome the inconsistency between experimental and numerical solution encountered in the work of Andersen *et al.* ([7]). Using a gas-kinetic scheme, the 2D Navier-Stokes equations were solved on a moving grid finding a good agreement with the experimental results.
Several authors have concentrated their attention on the understanding and prediction of the various

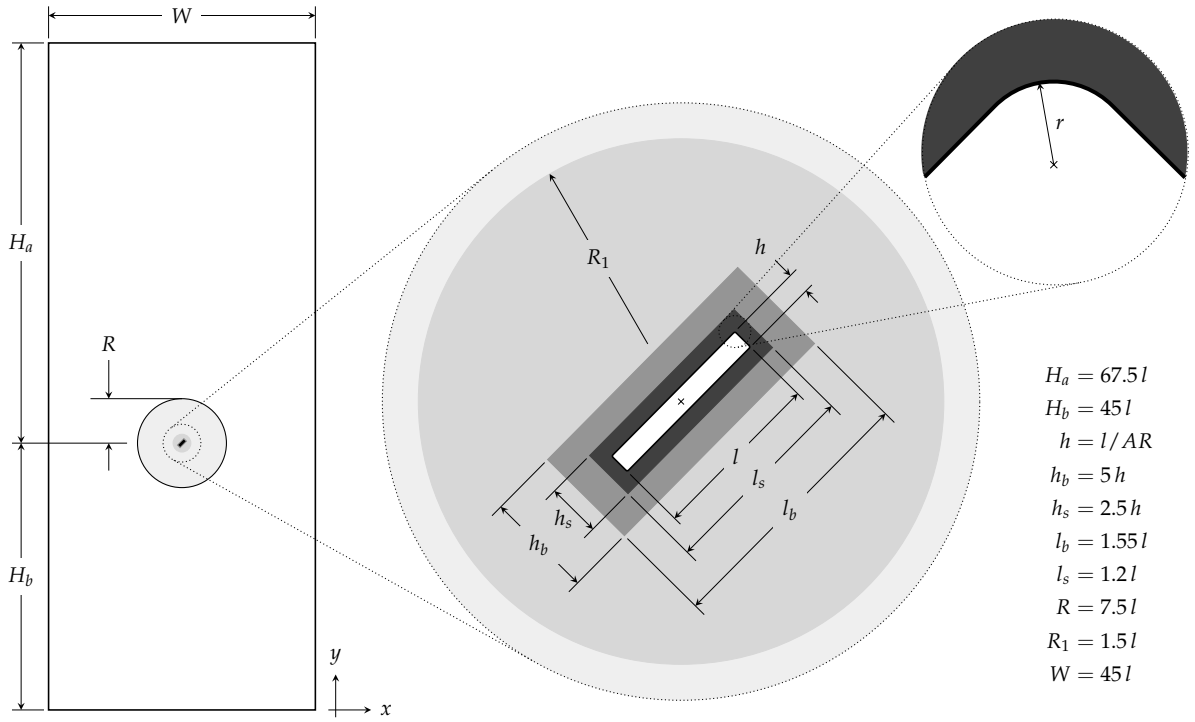

Figure 1: Computational domain and mesh refinement regions (in different colours). For the validation analysis the random variable r is considered equal to zero.

regimes [11, 12]. In this context the body shape is considered ideal, and no uncertainties in the input parameters are taken into account. In this work, we introduce a geometrical uncertainty: the fillet radius is treated as a random variable and, as a consequence, the fluid flow Navier-Stokes equations become stochastic. The Non-Intrusive Spectral Projection (NISP) method [13–15] computes the stochastic solution starting from the results of a series of deterministic solutions computed, in this case, using the commercial software STAR-CCM+. This paper is organized as follows. In the next section the governing equation are shown while in section 3 the validation study will be carried out. Afterwards, in section 4, the NISP method will be introduced and the stochastic results will be discussed in section 5. Finally, in section 6 we give our summary conclusions.

2 Problem Formulation and Geometrical Model

Our scope is to study the motion of a plate immersed in a fluid. Such a motion is evidently characterized by a fluid-body interaction. This implies that the motion of the plate is governed by both the fluid equations and the rigid body dynamic equations. Regarding the fluid, continuity and Navier-Sockes equations for incompressible flow are solved:

$$\nabla \cdot \boldsymbol{u} = 0 \qquad \frac{\partial \boldsymbol{u}}{\partial t} + (\boldsymbol{u} \cdot \nabla)\,\boldsymbol{u} = -\frac{1}{\rho}\nabla p + \nu \nabla^2 \boldsymbol{u} \tag{1}$$

where u is the velocity, t is the time, p is the pressure, ρ is the density and ν is the kinematic viscosity. The real motion of the body is governed by the cardinal equations of dynamics:

$$\boldsymbol{F} = m\frac{\mathrm{d}\boldsymbol{v}}{\mathrm{d}t} \qquad \boldsymbol{M} = \mathcal{I}\dot{\boldsymbol{\omega}} + \boldsymbol{\omega} \wedge \mathcal{I}\boldsymbol{\omega} \tag{2}$$

where m is the mass (considered constant), $\boldsymbol{v}$ is the velocity of the centre of mass and $\boldsymbol{F}$ is the resultant force acting on the body (that is, the sum of the buoyancy force and the aerodynamics forces), $\boldsymbol{\omega}$ is the angular velocity of the rigid body, $\boldsymbol{M}$ is the resultant moment acting on the body (due to fluid forces) and $\mathcal{I}$ is the tensor of the moments of inertia. Due to the 2D nature of this analysis, if a reference frame with its axes parallel to the body's principal axes of inertia is considered, the second cardinal equation simply becomes $M_z = \mathcal{I}_{zz}\dot{\omega}$.

In order to simulate the free fall of plates we resorted to the sliding mesh model. It consists of a plate fixed on a disk with radius R that can rotate with respect to the rest of the mesh (see Figure 1). To construct a universal domain for different plates size, all dimensions are proportional to the plate length l. In the same figure the various mesh refinement regions are represented by different colours.

Table 1: Comparison between experimental data form Andersen *et al.* [7] and numerical simulations.

	$\langle v_x \rangle [\mathrm{cm\,s^{-1}}]$	$\langle v_y \rangle [\mathrm{cm\,s^{-1}}]$	$\langle \omega \rangle [\mathrm{rad\,s^{-1}}]$	Descent angle [°]
Experiment [7]	15.9	−11.5	14.5	−35.8
Numerical [10]	15.1	−11.8	15.0	−38.0
Our model	15.6	−11.0	15.3	−35.2

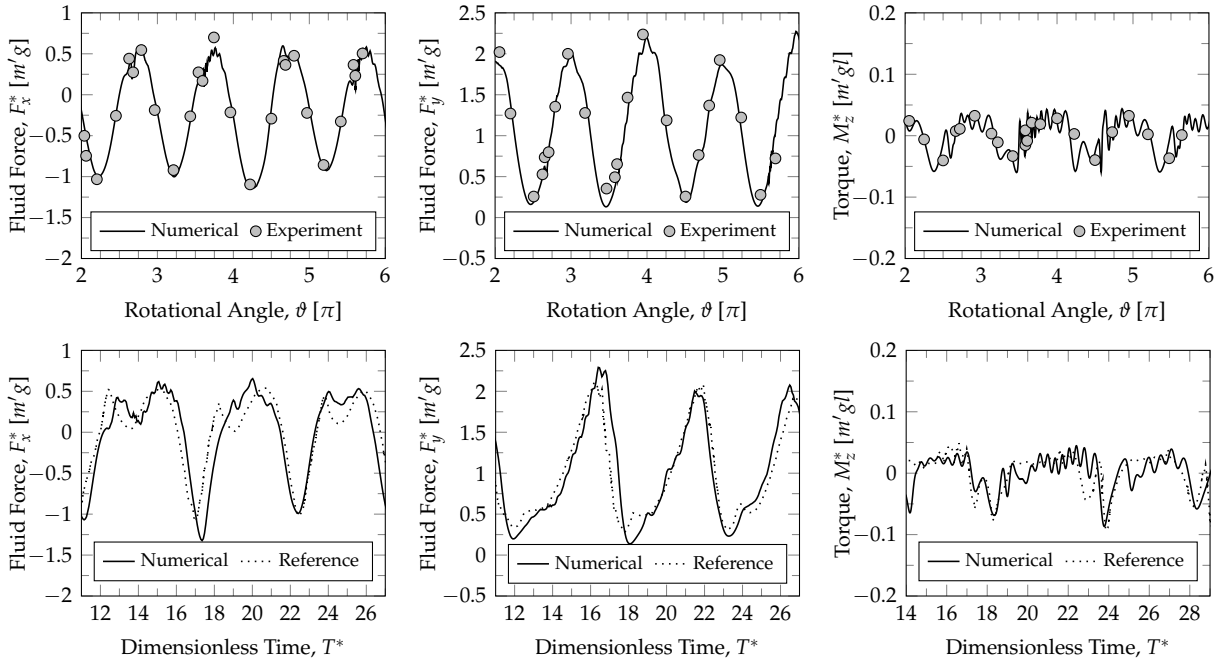

Figure 2: Fluid force and torque acting on the body. The results are compared with the experimental ones found by Andersen *et al.* [7] (on the top). On the bottom, the numerical work of Jin & Xu [10] is considered as reference.

In addition, on the plate surface the mesh is prismatic with a grid of 34×260 control volumes.

3 Validation

For the validation we took as reference the tumbling plate studied experimentally by Andersen *et al.* [7] which is the same plate Jin & Xu [10] used in their numerical analysis. The plate, which freely falls in water ($\rho_f = 1000\,\mathrm{kg\,m^{-3}}$ and $\nu = 8.8871 \times 10^{-7}\,\mathrm{Pa\,m}$), is an aluminium one ($\rho_b = 2700\,\mathrm{kg\,m^{-3}}$) of thickness ($h$) 0.81 mm and with an aspect ratio $AR = l/h$ of 8. The value of the acceleration due to gravity is $9.81\,\mathrm{m\,s^{-2}}$. Just as in [10], we assume that the body has an initial inclination of $\vartheta_0 = 45.3°$ with the horizon (counterclockwise rotations are considered positive) and an initial velocity (parallel to the major plate axis) of $12.615\,\mathrm{cm\,s^{-1}}$. In addition, a time step of $\Delta t = 2.5 \times 10^{-4}\,\mathrm{s}$ is used in order to minimize numerical errors in correspondence to the sliding mesh interface. For the validation, the fillet radius r of Figure 1 is assumed equal to zero.
In line with [7, 10], most of the results are represented in function of dimensionless parameters. The definition of these numbers is reported below:

$$U_t = \sqrt{2hg\left(\frac{\rho_b}{\rho_f} - 1\right)} \qquad T^* = t\frac{U_t}{l}$$
$$m' = (\rho_b - \rho_f)lh \qquad X^* = \frac{x}{l} \qquad (3)$$
$$Y^* = \frac{y}{l} \qquad F_i^* = \frac{F_i}{m'g} \qquad M_i^* = \frac{M_i}{m'gl}$$

where U_t is the average descent speed, obtained by balancing the buoyancy-corrected gravity, $m'g = (\rho_b - \rho_f)hlg$, with the quadratic drag, $\rho_f l U_t^2/2$. The other variables, namely T^*, X^*, Y^*, F^* and M^*, are respectively the dimensionless time, x coordinate, y coordinate, force and torque.
Simulations were carried out with STAR-CCM+ and the average results are shown in Table 1. Some discrepancies between numerical and experimental results still exist but the errors are in agreement with [10]. The independence of the mesh was checked by the use of two coarser meshes; this revealed how the velocities, as well as the descent angle, increase according to a typical exponential

law as the mesh becomes finer whereas the angular velocity decreases. Figure 3 illustrates the trajectory comparison of the numerical results with the experimental results as reported in [7]. The pattern found numerically is qualitatively equivalent to that found experimentally and the superimposition is quite good. Note how the trajectories do not start in the origin of the coordinate system: this is due to the fact that we are only interested in the periodic condition and in the first instants the motion of the plate is not well established.
The next step is to compare the dimensionless fluid forces and torque trends with the ones found in literature. Figure 2 shows the curve trend of F_x^* (on the top), F_y^* (on the bottom) in function of the plate angle ϑ (on the left) and of the dimensionless time T^* (on the tight). Our results fit quite well with the experimental points and, regarding F_x^*, the model finds correctly the oscillation of the minimum values. In the F_y plot there is a small discrepancy in the region of $3.5\,\pi$, where a little bit stronger force acts on the Andersen's plate. Regarding the comparison with the numerical results, the shapes of the curve are similar especially for the F_y. A small phase error exists but it is due to the small angular velocities difference that exists between the two numerical models: $15.0\,\mathrm{rad\,s^{-1}}$ found by the numerical analysis of Jin & Xu against our $15.3\,\mathrm{rad\,s^{-1}}$. The torque Figure **??** is characterized by very small values and it has qualitatively the same trend as the references. A high frequency oscillation exists and according to [8] and [10] this is because the moment is produced principally by the low pressure zones caused by the vortex shedding phenomena which characterized the wake.

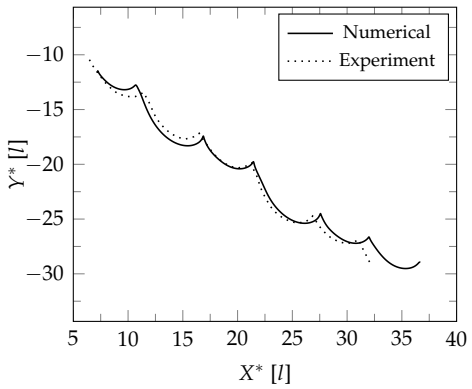

Figure 3: Trajectories comparison. The numerical results are compared with the experimental ones found by Andersen *et al.* [7]. As we can see, the two trajectories are quite similar.

4 Uncertainty Analysis

4.1 Geometries

The edge of an infinite rectangular body (the equivalent of the corner of a 2D shape) is considered as an uncertainty variable. Precisely, we assume that all corners are rounded by an arc of circle with a random radius r, sweeping from $r = 0$, corresponding to the rectangular shape, to $r = h/2$, that correspond to a perfectly semi-circular head. In addition, we assume that the four corners have the same radius value, therefore two axis of symmetry exist on the body. With these conditions, we have just one stochastic variable, r, and we assume all values inside the interval with the same probability.

4.2 Mathematical Formulation

Non-Intrusive Spectral Projection (NISP) method uses deterministic results for calculating the stochastic solutions. The specific mathematical model applied in this analysis will be described here. Let us consider r as the uncertain parameter of the model that is associated with the random variable ξ. Using a Polynomial Chaos expansion, is possible to express r in function of ξ:

$$r(\xi) = \sum_{n=0}^{q} \hat{r}_n \varphi_n(\xi) \tag{4}$$

where $\hat{r}_n$ are the expansion mode coefficients and φ_n are orthogonal polynomials of order n. As refereed in [16], depending on the PDF of r, there exists an optimal set of orthogonal polynomials φ_n associated with the random variable ξ that minimizes the required number of terms in the previous expansion. In this analysis, we considered a uniform distribution for r, therefore, the optimal set of orthogonal polynomials in (4) is given by the Legendre polynomials, defined by:

$$\begin{cases} \varphi_0(\xi) = 1 \\ \varphi_1(\xi) = x \\ \dots \\ \varphi_n(\xi) = \dfrac{(2n-1)}{n}\xi\varphi_{n-1}(\xi) - \dfrac{(n-1)}{n}\varphi_{n-2}(\xi) \\ \varphi_{n+1}(\xi) = \dfrac{(2n+1)}{n+1}\xi\varphi_{n-1}(\xi) - \dfrac{(n)}{n+1}\varphi_{n-1}(\xi) \end{cases} \tag{5}$$

In the previous definition, the random variable ξ is assumed to have a uniform distribution with zero mean and $1/\sqrt{3}$ standard deviation. Considering the Legendre polynomials, they have an important propriety which is the bedrock of the present formulation. They have the peculiarity to be orthogonal to each other with respect to the inner product in

Table 2: Comparison between the five different plates with different fillet radius.

	$\langle v_x \rangle$ [cm s^{-1}]	$\langle v_y \rangle$ [cm s^{-1}]	$\langle \omega \rangle$ [rad s^{-1}]	Descent angle [°]
r_1	15.2	−9.4	15.8	−31.7
r_2	15.0	−8.4	16.0	−29.2
r_3	13.8	−4.9	20.7	−19.6
r_4	12.5	−3.4	25.1	−15.2
r_5	12.0	−3.0	26.9	−14.0

the interval $[-1, 1]$:

$$\left\langle \varphi_i, \varphi_j \right\rangle = \int_{-1}^{1} \varphi_i \varphi_j W(\xi) \, \mathrm{d}\xi = \frac{1}{2j+1} \delta_{ij} \qquad (6)$$

where δ_{ij} is the Kronecker delta function and $W(\xi)$ is the weighting function of the probabilistic case which is equal to $1/2$.
Let us introduce a new variable, the solution of the system f, which in conformity with the previous considerations, is a function of ξ, $f(\xi)$. We can express it by using the Polynomials Chaos expansion (4) leading to:

$$f(\xi) = \sum_{j=0}^{Q} \hat{f}_j \varphi_j(\xi) \qquad (7)$$

where the $\hat{f}_j$ are the unknown expansion mode coefficients and – because we are just considering one uncertain variable (mono-dimensional case)– the total Q is equal to the highest Legendre polynomial considered.
If we multiply both sides of equation (7) by φ_k, calculate the inner product (6) and reorganize the terms, we get:

$$\hat{f}_k = \int_{-1}^{1} f \varphi_k \, \mathrm{d}\xi \, (2k+1) \qquad (8)$$

The previous integral will be estimated using the Gauss-Legendre quadrature:

$$\int_{-1}^{1} f \varphi_k \, \mathrm{d}\xi \approx \sum_{i=1}^{N_p} f(\xi_i) \, w_i \, \varphi_k(\xi_i) \qquad (9)$$

where ξ_i are the considered points which are found imposing the highest polynomials φ_{N_p} equal to zero, w_i the weights and $f(\xi_i)$ are the deterministic solutions found carrying out the simulations with the commercial software. Once the expansion coefficients $\hat{f}_k$ are known we can find the solution $f(\xi)$ from equation (7) and the correspondent PDF which, in this analysis, has been constructed using the kernel density estimation method [17].

5 Results

The uncertain quantification analysis is first performed on the tumbling plate and then the study is extended to the fluttering case. The objective is the same for the two different regimes. We are interested in plotting the ensemble average trajectory and in providing an estimation of the results for a confidence interval of 95%. In addition, we are looking for the PDF that describes the X^* solution when a specified Y^* is imposed, or in other words, the horizontal position after a fall from a specific height.

5.1 Tumbling Plate

The simulations were performed for a physical time of 5 s which correspond, in our condition, to a dimensionless time of 126.8 (see (3)). Figure 4 shows the five trajectories indicating that as the radius increases, the trajectories become more and more horizontal and the glides get smaller and smaller. This is as expected because the edges are less sharp and, as a consequence, less flow separation exists: the plate gains not only more lift but also it acts in a more constant manner which permits it to have a smoother and less inclined trajectory.

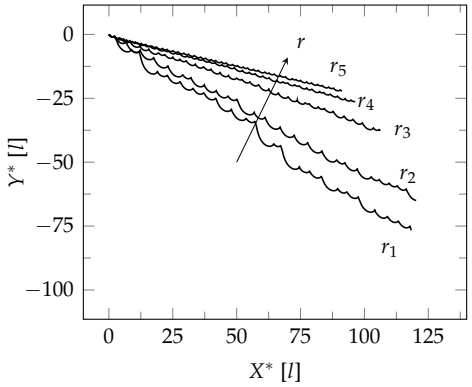

Figure 4: Trajectories for the tumbling plate when five different radii are considered. As beforehand, the falling angle decreases as the corners become less sharp.

Vortex shedding process still exists but it is not so strong (see Figure 5). As the radius become bigger, both the velocity along the x and y axis decrease while the average angular velocity increases. Table 2 lists the average results that are completely in accordance with those found during the code validation reported in Table 1.

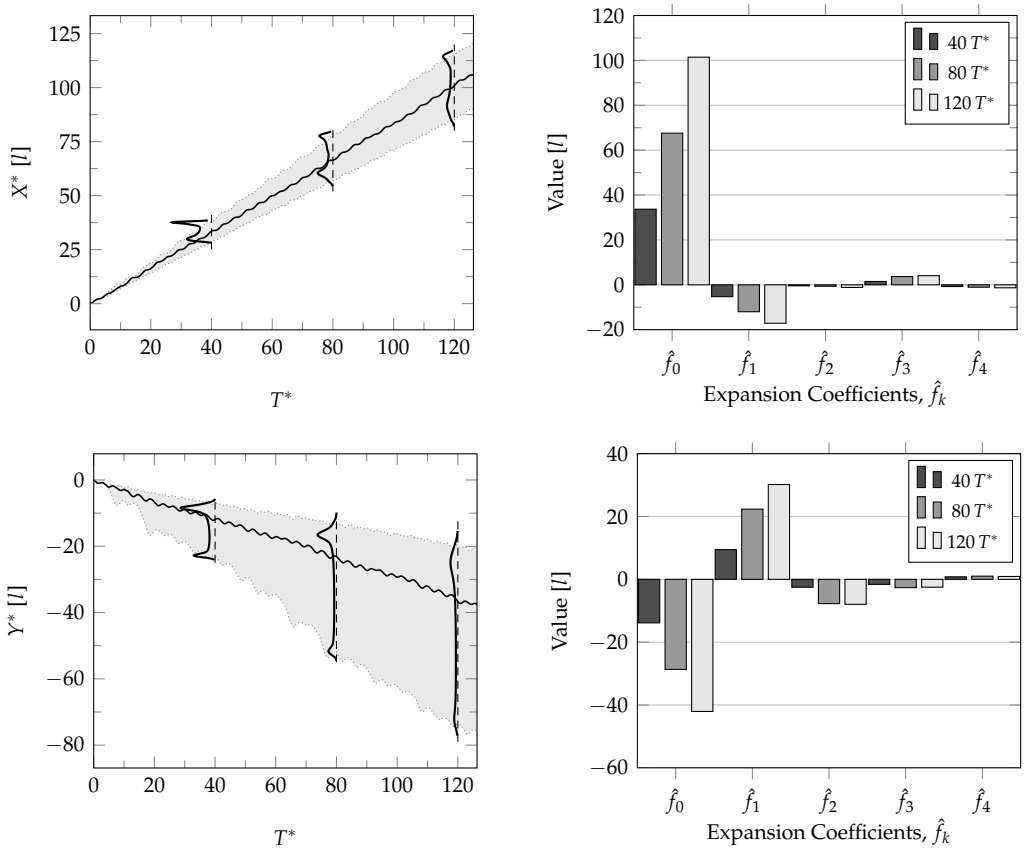

Figure 6: X^* and Y^* position in function of the time. The grey areas represents the uncertainty at which the plate is subjected while the black lines plots the median of PDF. In addition, PDFs are represented at three different instant. Note how in the shape exist two peaks which are getting smoother and smoother as the time increases. On the right, are shown the five coefficients of the solutions at which PDFs are drawn.

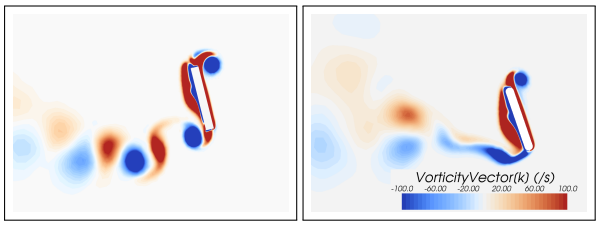

Figure 5: Vorticity field comparison around two tumbling plates. On the left the body has a small value of fillet radius while on the right the corner is more rounded.

Until now we have just described the deterministic results and no stochastic analysis has been done. Performing the uncertainty analysis, we get the results shown in Figure 6. Here, the stochastic solution is a function of the time and the grey area represents the uncertainty (with 95% confidence interval) of the X^* value. In correspondence to $T^* = 40$, $T^* = 80$ and $T^* = 120$, three PDFs of the solution at that instant are drawn. As we expected, they are characterized by a peak at each interval extremity: it is quite strong for low time values getting smoother and smoother as the time goes by until they almost become constant for high fillet radius value (the lower part). On a bar diagram the five coefficients of the solution at which previous PDFs are calculated are plotted. We can see how the stochastic mean, $\hat{f}_0$, is the main term and the coefficient of the linear polynomial, $\hat{f}_1$, plays an important role. The two-peaks shape, bimodal distribution, is given by the joint action of cubic and linear term contributions while the second and fourth order polynomials do not seem to enter in the polynomial chaos expansion. Since the higher order coefficients are quite small, we can assume that the convergence is reached and therefore further improvements would not modify significantly the PDFs shape.

Regarding the Y^* variable, the results obtained with the five points approximation are shown in Figure 6. The PDFs shape are equal to X^* solution, becoming almost constant for high time values. We can see how, in this case, the uncertainties are much bigger than the previous one. In correspondence to $T^* = 120$, the uncertainties enclose an interval of more than $60\,l$ in contrast with $35\,l$ of the X^* solution. The bar diagram shows how the modulus of the five coefficients is getting smaller and smaller as the polynomial grade increases. As beforehand, we can assume that the convergence is reached.

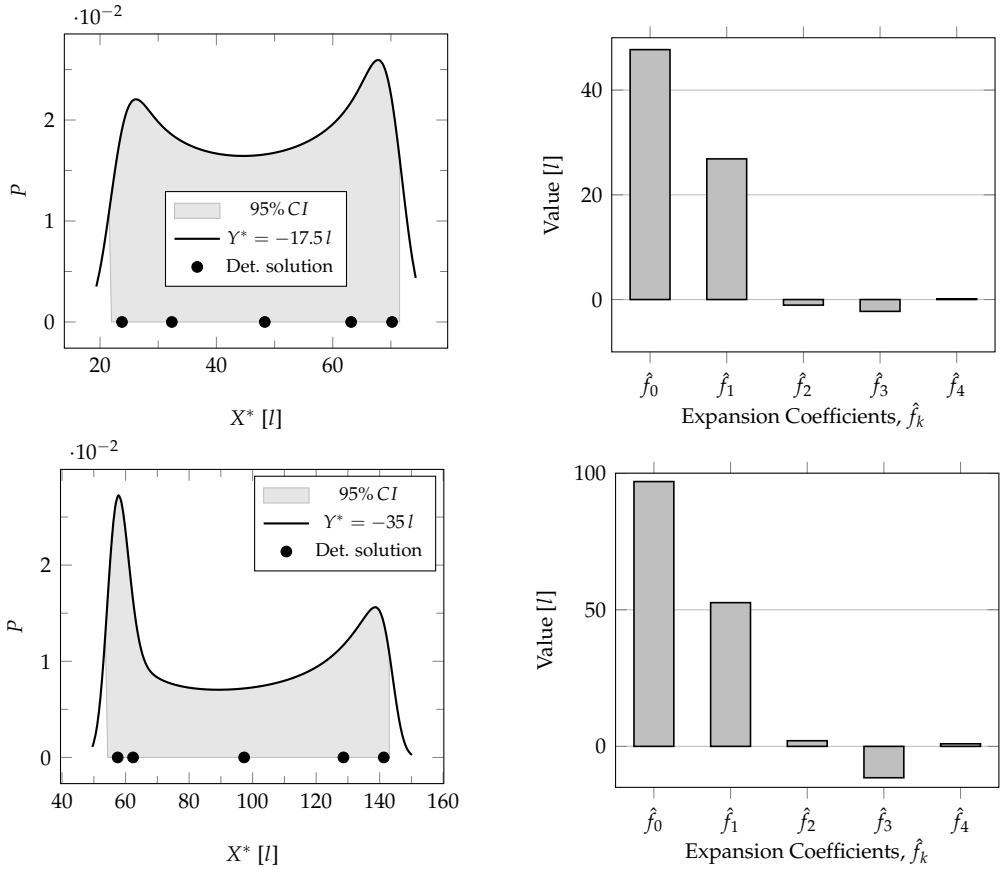

Figure 7: X^* position after a fall of $17.5\,l$ (top) and $35\,l$ (bottom). On the left, the PDFs trend and the respective confidence intervals (grey areas). Deterministic solutions are also plotted. On the right, we find the various expansion coefficients.

One of the objectives of this study is to find the PDF that describes the X^* solution when a prescribed fall is imposed. A fall of $Y^* = -17.5\,l$ and another of $Y^* = -35\,l$ are considered. From Figure 4 it is possible to note how the r_4 and r_5 plate do not reach the lower Y^* coordinate, so an extension of the physical time until 7 s ($T^* = 177.6$) and 8 s ($T^* = 202.9$) was needed.
Figure 7 shows the results for the two different falls. On the top, is reported the PDF for the small fall, *i.e.* after a vertical distance of $17.5\,l$ while on the bottom the solution for $Y^* = -35\,l$. The two PDFs are quite similar, both are bimodal and their values decrease in the centre. The particular shape is in accordance with the deterministic solutions, also shown in the same plot with black points. Besides the PDFs, the plots reports the confidential interval of 95%, represented with the shadowed areas. On the right are plotted the expansion coefficients in a bar diagram showing how the importance of the high order polynomials is getting less and less important and almost vanished in correspondence to the fourth order. Hence, we supposed that the convergence is reached and we can conclude that the system does not follow a linear law, but a concentration of events exist with respect to the interval's extremes.

5.2 Fluttering Plate

According to [7], fluttering motion is observed if the length of the plate l is increased in such a way that the aspect ratio AR is equal to 14 and all the other dimensional parameters are kept constant.
The simulation were carried out using a fixed time step of $\Delta t = 5 \times 10^{-4}$ s.

The objectives of the analysis of the plate under flutter are to find the ensemble average trajectory, the associated confidential interval and the plate position after a fall of specific height.
Figure 9 shows the 5 deterministic trajectories of the plate. Before analysing the results through a stochastic point of view and conducting the convergence study, we notice that the centre of mass elevation points, after the first glide, appear sequentially and in an almost linear manner as the fillet radius increases. However, after the second glide, the path relative to the plate with fillet radius r_4 stays between the r_1 and r_2 trajectories and not, as we would have expected, between r_3 and r_5. In order to understand this anomaly, the interval between r_3 and r_4 was subdivided in four equally

spaced parts, calling the nodes in between r_{334}, r_{34} and r_{344} while we introduce just one point, r_{45}, in the interval $[r_4, r_5]$ which coincides with the interval's middle point (see Figure 8). Simulations were performed with these new values of fillet radius and the results confirm the anomaly, highlighting how the locus of the peak points initially increases its ordinate value in an almost linear manner. Afterwards, the curve inverts the trend going backwards and reaching its minimum X^* value with r_{344} before taking one more time the right direction and, after r_4, an apparently linear behaviour appears. The previous consideration can be well appreciated in Figure 10: a black line helps to follow the curve peaks of the various trajectories.

In order to find a physical explication of this behaviour, the vorticity field around the plates was observed. We took as reference models the plates with fillet radius equal to r_3, r_{344} and r_{45}. To complete the study, three different time instants were considered: the first, t_1 is when the plate stays in the horizontal position, *i.e.* the local and the global reference frames are superimposed; in the second instant, t_2, the plate is at the maximum centre of mass elevation point and, the third one t_3 is considered equal to $t_3 = t_2 + (t_2 - t_1)$. Results are shown in Figure 11. Observing the pictures we notice how the interaction between vortexes and body exists especially when the body starts to descend. Let us analyse the images placed in the first row: the vorticity field appear very similar, but small differences in the wake structure can be be observed between the three pictures. Regarding the second row, these differences become more accentuated and the vorticity field assume another pattern: the r_3 plate has the vortex which is shedding on the upper part of the trailing edge, in the centre plates it is on the lower side and in r_{45} plate the vortex placed on the lower side has just detached. Since the vorticity is directly bound to the velocity's field, it means that the pressure field is different, therefore the forces acting on the body will have some variations.
Coming back to the stochastic analysis, five or more deterministic solutions are few to ensure convergence. We noticed that as the polynomial grade increases, the coefficients become higher and higher, therefore, we are very far from the convergence. As a consequence, we would need much more points in order to properly analyse the flattering plate. An alternative is to restrict the interval of the radius random variable r.
The initial interval $[0, h/2]$ was subdivided into four equal parts and the analysis was performed with 9 points in $[0.75\frac{h}{2}, \frac{h}{2}]$ to avoid the interval in which peaks inversion phenomena occurs. The number of sample suggests that 36 points are not enough to ensure convergence and a very large number of samples (hundreds) is required. This is due the fact that a small perturbation causes a large variability of the trajectory path requiring a large number of degrees of freedom in order to stochastically analyse the problem.
The computing time for 155×10^3 control volumes and 10^4 time steps is around 75 CPU hours for each unsteady deterministic calculation, consequently the problem can only be treated with high performing computing. Previous investigation [7, 9, 11] have reported that the regimes of 2D free fall plate can be tumbling, fluttering, steady fall and chaotic regime with a mixture of tumbling and fluttering. The present case of perturbation of the fluttering regime undergoes a chaotic path trajectory preserving the fluttering motion.

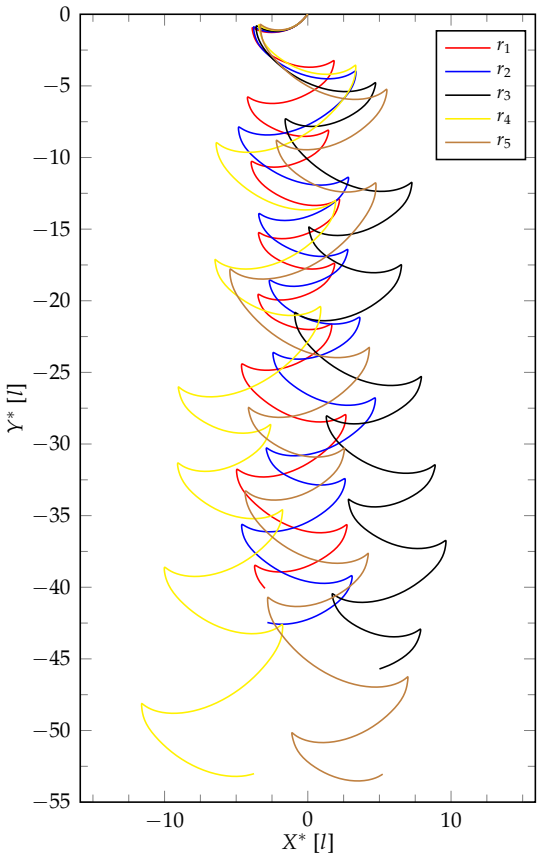

Figure 9: Fluttering case. Path obtained with five different fillet radius values.

In order to understand the importance of the vortex shedding in the fluttering regime, three plates were considered at rest and simulations were carried out. The bodies are aligned with the flow that has a velocity magnitude of $0.35\,\mathrm{m\,s^{-1}}$, that is a typical velocity in the fluttering regime. In this case the Reynold's number is equal to $\mathrm{Re} = 4466$ while, during the fall, it can vary between 200 and 5800. The considered plates present a fillet radius that are, in percentage of $\frac{h}{2}$, $r_1 = 1.59\%$ (it is the first of the 9 Gauss points, chosen to avoid the 90 degree corner), $r_2 = 50\%$ and $r_3 = 100\%$. Figure 12

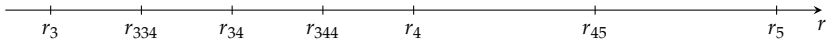

Figure 8: In order to investigate the anomaly of the trajectories, the interval between r_3 and r_4 is divided in four equal intervals while the one between r_4 and r_5 has just one point in the middle, r_{45}.

shows that as the corners become less sharp, the force amplitude decreases while the frequency increases by a non-linear law. The forces developed by the sheds of the vortices represent a percentage that can reach up to 23% of the total fluid force for small fillet radius while the value reduces to 10% for a completely round head. However the frequency is always higher than the characteristic frequency of the motion of about 20 times. For higher velocities, the phenomena become stronger and both the amplitude and the frequency increase. In any case, the variability of the vortex shedding is added to the variability of both the mass and the moment of inertia, that all contribute to the dynamic of the plate. The critical zone is in the nearby to the peak points, in which small perturbations can slightly modify the plate inclination, causing macro differences in the trajectory path.

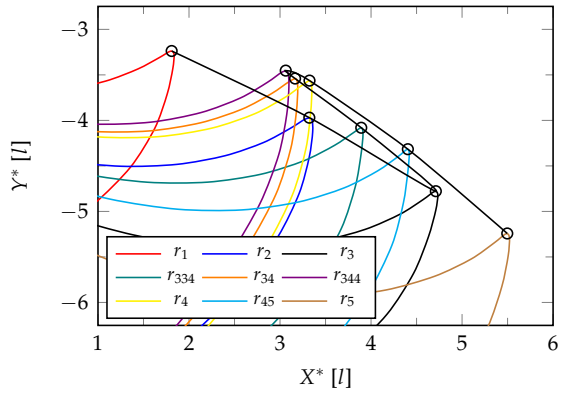

Figure 10: The solution for intermediate cases shows the peaks anomaly and a black line marks the its locus of points.

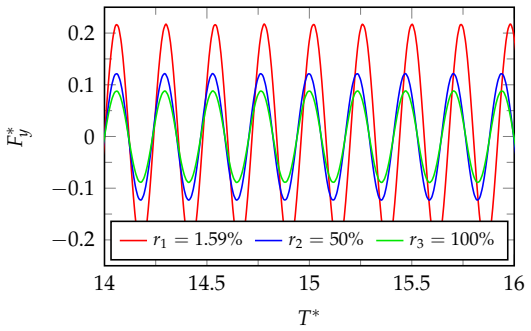

Figure 12: Dimensionless forces developed by vortex shedding in function of dimensionless time on three fluttering plates immersed in a frontal flow with magnitude $0.35\,\mathrm{m\,s^{-1}}$. As the fillet radius increases, the amplitude decreases and the frequency increases.

6 Conclusions

Through the results obtained in this work, several conclusions can be drawn.
The adopted numerical methodology provided realistic results for two-dimensional tumbling plate and the model can correctly predict the trajectory, the forces and the torque acting on the body. The predictions are in good agreement with experimental data; results confirm and give details on how the wake is governed by a vortex shedding process.
In the tumbling case, the fillet corner highly modifies the trajectory mean angle and angular rotation modulus. We ascribe this fact to the different wake structure caused by the different corner sharpness, which originate different flow separation processes.
In fluttering, the locus of the second glide peaks displays an unexpected behaviour for r included in the interval $[0.50\frac{h}{2}\ 0.77\frac{h}{2}]$. The wake examination reveals that the vorticity field around the plate is characterized by a wake-body interaction which perturbed the trajectories.
In tumbling motion five points are sufficient to find correctly the solution with the NISP approach, and results show the bimodal trajectory and the increasing error bar.
In the fluttering regime, a much higher number of deterministic solutions is required. The system is characterized by a great variability and small perturbations in the geometry shape (input) cause large variations in the trajectory (output) underlying how the system is strongly non-linear. After the second glide, an apparently chaotic behaviour is observed that can be clarified with stochastic calculations but require a prohibit number of simulations.

References

[1] C. K. Augspurger. “Morphology and dispersal potential of wind-dispersed diaspores of neotropical trees”. In: *American Journal of Botany* 73.3 (1986), pp. 353–363.

[2] James Clerk Maxwell. “On a particular case of the descent of a heavy body in a resisting medium”. In: *Cambridge and Dublin Mathematical Journal* 9 (1854), pp. 145–148.

[3] Paul Dupleich. *Rotation in Free Fall of Rectangular Wings of Elongated Shape*. Tech. rep. 1201. NACA, 1941.

[4] H. J. Lugt. “Autorotation of an elliptic cylinder about an axis perpendicular to the flow”. In: *Journal of Fluid Mechanics* 99.04 (1980), pp. 817–840.

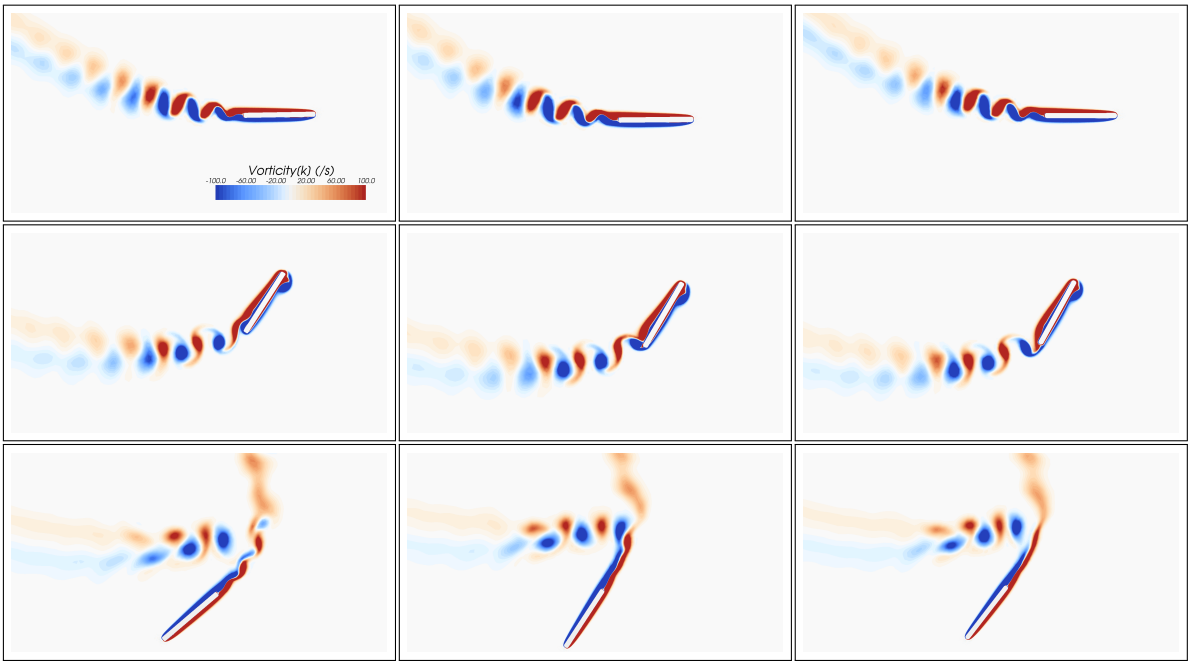

Figure 11: Vorticity field around the fluttering plate. **(a)**, **(b)** and **(c)** are respectively the solution of r_3, r_{344} and r_{45}. From this picture we can see how the vortex shedding process interacts with the body.

[5] H J Lugt. "Autorotation". In: *Annual Review of Fluid Mechanics* 15.1 (1983), pp. 123–147.

[6] Andrew Belmonte, Hagai Eisenberg, and Elisha Moses. "From Flutter to Tumble: Inertial Drag and Froude Similarity in Falling Paper". In: *Phys. Rev. Lett.* 81 (2 1998), pp. 345–348.

[7] A. Andersen, U. Pesavento, and Z. Jane Wang. "Unsteady aerodynamics of fluttering and tumbling plates". In: *Journal of Fluid Mechanics* 541 (2005), pp. 65–90. ISSN: 1469-7645.

[8] Rajat Mittal, Veeraraghavan Seshadri, and Holavanahalli S. Udaykumar. "Flutter, Tumble and Vortex Induced Autorotation". English. In: *Theoretical and Computational Fluid Dynamics* 17.3 (2004), pp. 165–170. ISSN: 0935-4964.

[9] Umberto Pesavento and Z. Jane Wang. "Falling Paper: Navier-Stokes Solutions, Model of Fluid Forces, and Center of Mass Elevation". In: *Phys. Rev. Lett.* 93 (14 2004), p. 144501.

[10] Changqiu Jin and Kun Xu. "Numerical Study of the Unsteady Aerodynamic of Freely Falling Plates". In: *Comunication in Computational Physics* 3.4 (2008), pp. 834–851.

[11] A. Andersen, U. Pesavento, and Z. Jane Wang. "Analysis of transitions between fluttering, tumbling and steady descent of falling cards". In: *Journal of Fluid Mechanics* 541 (2005), pp. 91–104. ISSN: 1469–7645.

[12] S. B. Field, M. Klaus, M. G. Moore, and F. Nori. "Chaotic dynamics of falling disks". In: *Nature* 388 (1997), pp. 252–254.

[13] Dongbin Xiu and George Em Karniadakis. "Modeling uncertainty in flow simulations via generalized polynomial chaos". In: *Journal of Computational Physics* 187.1 (2003), pp. 137 –167. ISSN: 0021-9991.

[14] M.A.A. Mendes, S. Ray, J.M.C. Pereira, J.C.F. Pereira, and D. Trimis. "Quantification of uncertainty propagation due to input parameters for simple heat transfer problems". In: *International Journal of Thermal Sciences* 60 (2012), pp. 94 –105. ISSN: 1290-0729.

[15] M.A.A. Mendes, J.M.C. Pereira, and J.C.F. Pereira. "Calculation of premixed combustion within inert porous media with model parametric uncertainty quantification". In: *Combustion and Flame* 158.3 (2011), pp. 466 –476. ISSN: 0010-2180.

[16] Dongbin Xiu and George Em Karniadakis. "The Wiener–Askey polynomial chaos for stochastic differential equations". In: *SIAM Journal on Scientific Computing* 24.2 (2002), pp. 619–644.

[17] Alan Julian Izenman. "Recent Developments in Nonparametric Density Estimation". In: *Journal of the American Statistical Association* 86.413 (1991), pp. 205–224. ISSN: 01621459.